

Chapter 9

A continuum model for the dynamics of the phase transition from slow-wave sleep to REM sleep

J.W. Sleigh, M.T. Wilson, L.J. Voss, D.A. Steyn-Ross, M.L. Steyn-Ross, and X. Li

9.1 Introduction

The cortical transition from the slow-wave pattern of sleep (SWS) to the rapid-eye-movement (REM) pattern is a dramatic feature of the somnogram. Indeed, the change in the electrocorticogram (ECoG) is so abrupt that the moment of transition usually can be identified with a time-resolution of about one second [8, 37]. Although the neuromodulatory environment and electroencephalographic patterns recorded during the steady states of SWS and REM have been well described [16, 30], the dynamics of the transition itself has been described only in a qualitative observational fashion [12], and has not been the focus of detailed quantitative modeling.

In SWS, the rat cortex shows predominant activity in the delta ($\sim 1\text{--}4$ Hz) band. This pattern shifts to an intermediate sleep state (IS)—sometimes termed “pre-REM”—where the cortical activity shows features of both SWS and REM, lasting 10–30 seconds [7, 12, 25, 28]. This is followed by an abrupt transition to the REM state, characterized by strong theta ($\sim 5\text{--}8$ Hz) oscillation [2], and loss of delta power. The main effector of the cortical transition from SWS to REM is believed to be a linear progressive increase in cholinergic input into the cortex from the brainstem (mainly from the pedunculo-pontine tegmentum area), acting via the thalamus or basal forebrain [18, 34].

Jamie W. Sleigh · Logan J. Voss

Department of Anaesthesia, Waikato Clinical School, University of Auckland, Waikato Hospital, Hamilton 3204, New Zealand.

e-mail: sleighj@waikatodhb.govt.nz VossL@waikatodhb.govt.nz

Marcus T. Wilson · D. Alistair Steyn-Ross · Moira L. Steyn-Ross

Department of Engineering, University of Waikato, P.B. 3105, Hamilton 3240, New Zealand.

e-mail: m.wilson@waikato.ac.nz asr@waikato.ac.nz msr@waikato.ac.nz

Xiaoli Li

School of Computer Science, The University of Birmingham, Edgbaston, Birmingham, B15 2TT, UK. e-mail: X.Li@cs.bham.ac.uk

Several studies [8, 32, 37] have measured the activity of the cortically-projecting pontine cholinergic REM-on neurons during the SWS–REM transition. These studies have shown a progressive, linear increase in firing rate, starting 10–60 s before onset of REM sleep, and plateauing about 60 s after transition. The predominant effect of increasing cholinergic input is to raise cerebral cortical arousal by acting on muscarinic (mainly M1) receptors to close potassium channels, causing a depolarizing shift in the cortical resting membrane potential. The increase in cholinergic tone also results in a small decrease in the amplitude of the excitatory postsynaptic potential (EPSP) [13, 23, 27].

A recent paper by Lu and others has highlighted the fact that the pontine cholinergic nuclei are themselves under the influence of other orexinergic and gamma-aminobutyric acid (GABA)-ergic switching circuits [24]. They suggest that the “flip-flop” arrangement of these brainstem and midbrain circuits could explain the abrupt changes in state observed in the cortex.

In contrast, we suggest that the abrupt changes seen in ECoG during SWS-to-REM transition could be explained in terms of an abrupt cortical response to a gradual change in the underlying subcortical neuromodulator activity. As described below, we enhance a previously-published continuum model of interactions between excitatory and inhibitory populations of cortical neurons [39, 40, 47–49], and compare its output with experimentally-derived data recorded from rats during the SWS-to-REM transition.

9.2 Methods

9.2.1 Continuum model of cortical activity

We use a continuum model of the interactions between populations of inhibitory and excitatory cortical neurons to describe the features of the SWS-to-REM transition. The continuum (or mean-field) approach assumes that the important dynamics of neuronal activity can be captured by the averages of small populations of ($\sim 10\,000$ – $100\,000$) neurons contained within a “macrocolumn” (defined by the spatial extent of the typical pyramidal neuron’s dendritic arborization). Continuum modeling of the cortex originated with Wilson and Cowan [46], and has been progressively refined since then by the inclusion of more neurobiologically realistic terms and parameters [22, 39, 50].

Our version of the model has been described in detail by Wilson *et al.* [49]. It is cast in the form of a set of stochastic differential equations; these equations incorporate (i) spike-rate input from: neighboring cortical neurons (dependent on local membrane potential), distant cortical neurons (dependent on distant membrane potential), and subcortical structures (independent of cortical membrane potential); (ii) dendritic time-evolution and magnitudes of fast inhibitory and excitatory synaptic potentials (including the effects of reversal potentials); (iii) a sigmoid

relationship between soma potential and neuronal firing rate; and (iv) cortical connectivity that drops off (approximately exponentially) with increasing spatial separation. The mathematical details of the theoretical model are outlined in the Appendix.

In general, parameter values are drawn from experimentally-derived measurements reported in the literature, so are physiologically plausible. The actual values used here are similar to those presented in an earlier paper modeling the seizurogenic effects of enflurane in humans [47], with some alterations to better represent the smaller rat cortex (see Table 9.1).

Table 9.1 Parameters for rat cortex model

Symbol	Description	Value
$\tau_{e,i}$	Membrane time constant	20, 20 ms
$Q_{e,i}$	Maximum firing rates	60, 120 s ⁻¹
$\theta_{e,i}$	Sigmoid thresholds	-58.5, -58.5 mV
$\sigma_{e,i}$	Standard deviation of thresholds	4, 6 mV
$\rho_{e,i}$	Gain per synapse at resting voltage	0.001, -0.000863 mV s
$V_{e,i}^{\text{rev}}$	Cell reversal potential	0, -70 mV
$V_{e,i}^{\text{rest}}$	Cell resting potential	-64, -64 mV
N_{eb}^{α}	Long-range $e \rightarrow e, i$ connectivity	3710
N_{eb}^{β}	Short-range $e \rightarrow e, i$ connectivity	410
N_{ib}^{β}	Short-range $i \rightarrow e, i$ connectivity	800
$\langle \phi_{eb}^{\text{sc}} \rangle$	Mean $e \rightarrow e, i$ subcortical flux	50 s ⁻¹
$\langle \phi_{ib}^{\text{sc}} \rangle$	Mean $i \rightarrow e, i$ subcortical flux	50 s ⁻¹
γ_{eb}	Excitatory synaptic rate constant	949 s ⁻¹
γ_{ib}	Inhibitory synaptic rate constant	100 s ⁻¹
$L_{x,y}$	Spatial length of cortex	2 cm
Λ_{eb}	Inverse-length connection scale	0.4 mm ⁻¹
v	Mean axonal conduction speed	1400 mm s ⁻¹
ΔV_e^{rest}	Effect of altering extrasynaptic ion channels	-5 → +5 mV
λ	Scaling for EPSP amplitude	see Eqs (9.2, 9.3)

The primary output from the model is the spatially-averaged soma potential. The fluctuation of this voltage with time is assumed to be the source of the experimentally observable ECoG signal [50]. In its present form, the model considers the cortex to be a two-dimensional sheet; the model ignores within-cortex microanatomical layering, and does not include synaptic plasticity. (The dynamic implications of these finer biological details may be the subject of future investigation.)

The changes in interneuronal population activity during sleep can be represented on a two-parameter domain (see Fig. 9.1), chosen to make explicit the effects of selected neuromodulators on the cortex. It is assumed that these neuromodulations are slow processes (\sim seconds to minutes) compared to the much faster time-scale of synaptic neurotransmission and conduction of action potentials (\sim ones to tens of milliseconds).

This separation of time-scales allows neuromodulator action to be incorporated into the model as a pair of slowly-varying control parameters that represent excursions along the mutually-orthogonal horizontal directions in Fig. 9.1 labeled, respectively, λ and ΔV_e^{rest} . Here, λ represents EPSP synaptic strength, and ΔV_e^{rest} represents relative neuronal excitability (displacement of resting membrane potential of the pyramidal neurons relative to a default background value).

This arrangement allows the effects of neuromodulators on synaptic function (the λ -axis) to be separated from their effects on extrasynaptic leak currents that will alter resting voltage (ΔV_e^{rest} -axis). We assume that SWS is associated with decreased levels of aminergic and cholinergic arousal from the brainstem, together with elevated concentrations of somnogens such as adenosine [31]; both effects will tend to hyperpolarize the membrane voltage by increasing outward potassium leak current.

The gradual rise in neuromodulator-induced membrane polarization is incorporated into the model as a slowly-increasing ΔV_e^{rest} parameter (see Eq. (9.1) below) that can be visualized as a trajectory (thick gray arrow) superimposed on the Fig.-9.1 manifold of stationary states. The mean excitatory soma potential V_e is depicted

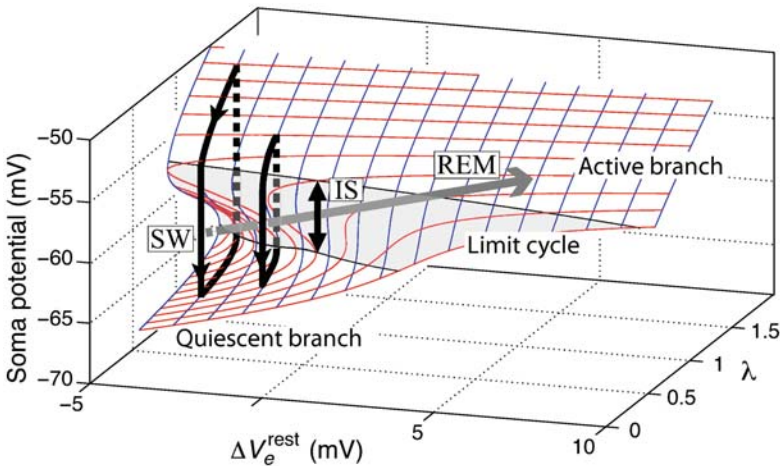


Fig. 9.1 Manifold of equilibrium states for homogeneous model cortex for different stages of sleep. Vertical axis is excitatory soma potential; horizontal axes are λ (dimensionless EPSP-amplitude scalefactor), and ΔV_e^{rest} (deviation of resting membrane potential above default value of -64 mV). Shaded-gray area shows region of instability giving rise to theta-frequency limit-cycle oscillations. The gray arrow shows a trajectory for transition from slow-wave (SW) to intermediate (IS) to REM sleep caused by a gradual increase in resting soma potential (see Eq. (9.1)). Black arrows denote the details of the trajectory in response to the dynamic modulation in EPSP (Eq. (9.3)).

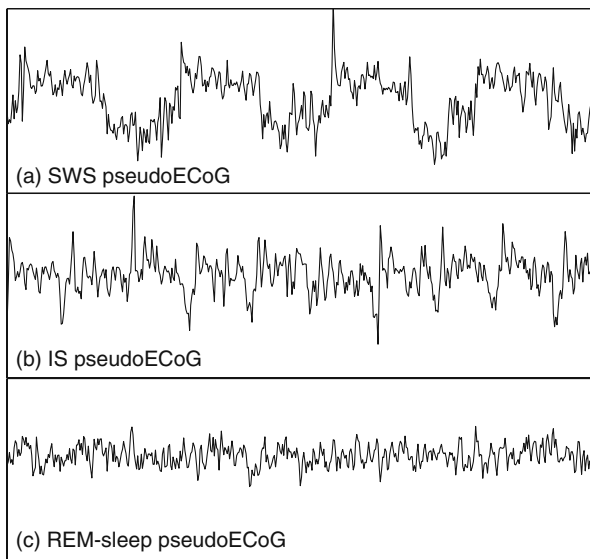


Fig. 9.1 (*cont.*) Model-generated ECoG time-series at the three labeled points on the sleep manifold: (a) slow-wave sleep (SWS); (b) intermediate sleep (IS); (c) rapid-eye-movement (REM) sleep. Duration of each time-series = 6 s; vertical-axis extent for each graph = 0.4 mV.

on the vertical axis of Fig. 9.1. Where there is a “fold” in the manifold, there can exist up to *three* steady-state values for V_e at a given $(\lambda, \Delta V_e^{\text{rest}})$ coordinate: for these cases we label the lower state (lying under the fold) as “quiescent”, and the upper state (located on top of the fold) as “active”. We note that the upper and lower stationary states are *not necessarily stable*. In fact, it is the transition to instability that gives rise to oscillatory behavior in the model.

9.2.2 Modeling the transition to REM sleep

The transition to REM sleep is characterized by a progressive increase in cholinergic activity from the brainstem that occurs over a time-course of a few minutes. This increase in cholinergic tone simultaneously depolarizes the cortex, and reduces (slightly) the excitatory synaptic gain (via reduction in the area of the excitatory postsynaptic potential (EPSP)). We model the gradual rise in cortical depolarization by imposing a linear increase in the excitatory resting-potential *offset* ΔV_e^{rest} , from -5 mV (i.e., resting voltage set 5 mV *below* nominal) to $+5$ mV (resting voltage set 5 mV *above* nominal), over a period of 4 min (240 s),

$$\Delta V_e^{\text{rest}}(t) = -5 \text{ mV} + 10 \text{ mV}(t/240 \text{ s}), \quad (9.1)$$

where t is the elapsed time in seconds. The nominal resting voltage is -64 mV (see Table 9.1). At the same time, the EPSP gain-factor λ_1 (dimensionless) decreases

linearly over 4 min to its nominal value ($\lambda_1 = 1.00$) from a starting value set 5% above nominal,

$$\lambda_1(t) = 1.05 - 0.05(t/240 \text{ s}). \quad (9.2)$$

Here, λ_1 is modeling the synaptic effect of the steady increase of acetylcholine concentration as the cortex transits from SWS to REM sleep. This slow acetylcholine change (λ_1) will be combined with the synaptic-gain adaptations (λ_2), described below, brought about by the SWS cortical oscillations between “down” and “up” states.

9.2.3 Modeling the slow oscillation of SWS

Because slow-wave sleep is characterized by low levels of cholinergic tone, the excitatory synaptic gain in the cortex is influenced by the presynaptic firing-rate, resulting in a form of slow spike-frequency adaptation: when the presynaptic neuron is in a high-firing state, consecutive EPSP events decrease in magnitude exponentially over the time-course of a few-hundred milliseconds as described by Tsodyks [43]; conversely, once the presynaptic neuron becomes quiescent, it becomes relatively more sensitive to input. Under conditions of low-cholinergic effect, this fluctuation in excitatory synaptic gain induces the cortex to undergo a slow oscillation between the distinct “down” (quiescent) and “up” (activated) states that are observed in SWS [26, 38]. This approach to understanding the cortical slow oscillation is broadly equivalent to previous SWS models [1, 6, 14, 17, 33, 36, 41] which rely on time-varying changes in the Na^+ and K^+ ion-channel conductances to cycle the cortex between “up” and “down” states.

This up–down cycling is in addition to the slower modulation due to brainstem changes (Eq. (9.2)), so we write the total synaptic-gain factor as $\lambda = \lambda_1 + \lambda_2$, where λ_1 corresponds to very slow brainstem effects, and λ_2 to the slow-oscillation effects. We drive parameter λ_2 through a cycle between down- and up-states by raising λ_2 (increasing EPSP) slightly in response to a low firing rate, and reducing it (lowering EPSP) in response to a high firing rate,

$$\frac{d\lambda_2}{dt} = -k(\lambda_2 - \lambda_{\text{aim}}), \quad (9.3)$$

where the shunting rate-constant k is 2 s^{-1} , and the steady-state target value λ_{aim} is determined by the firing rate,

$$\lambda_{\text{aim}} = \begin{cases} +0.2, & Q_e < 10 \text{ s}^{-1}, \\ -0.2, & Q_e \geq 10 \text{ s}^{-1}. \end{cases} \quad (9.4)$$

The full set of cortical equations are listed in the Appendix on p.215. The total synaptic gain $\lambda = \lambda_1 + \lambda_2$ from Eqs (9.2–9.3), and the ΔV_e^{rest} depolarization from Eq. (9.1), are applied as modulatory effects to the differential equation for excitatory soma potential (Appendix, Eq. (9.5)). The model behavior resulting from the cycling and modulation in λ , and the modulation of ΔV^{rest} , is summarized by the arrowed paths in Fig. 9.1.

9.2.4 Experimental Methods

9.2.4.1 Animals

Four male Sprague-Dawley rats, weighing 300–400 g at the time of surgery, served as subjects. The rats were maintained on a 12:12-hr light–dark cycle, were individually housed following surgery, and had *ad libitum* access to food and water. Ethical approval for this study was granted by the Ruakura and University of Auckland Animal Ethics Committees.

9.2.4.2 Surgery

Animals were anesthetised with ketamine/xylazine (75/10 mg/kg, i.p.), and mounted in a stereotaxic instrument with the skull held level. Four holes were drilled in the exposed skull: three for stainless-steel skull screws (positioned over the cerebellum and bilaterally over the parietal cortex), and one for implantation of a tungsten stereotrode pair (Micro Probe Inc, Potomoc, USA) into the parietal cortex for two-channel electrocorticogram (ECoG) recording. The stereotrode consisted of two insulated microelectrodes (3- μm diameter) separated by 200 μm . The stereotrode was lowered into the cortex to a depth of 0.5 mm and cemented to one of the anchor screws with rapid-setting glue. The skull screws also served as reference and ground electrodes for the cortical local-field-potential recordings. Insulated wires from the screws, along with the stereotrode electrodes, were terminated in a plastic nine-pin socket, the base of which was embedded in dental acrylic (GC Corporation, Tokyo, Japan). The animals were allowed to recover for at least seven days prior to testing.

9.2.4.3 Data recording

There were two ECoG recording channels. The two parietal skull screws served as the common reference for the two cortical electrodes, and the cerebellar screw was used as the common ground. The leads were connected to two differential amplifiers (A-M systems Inc, Carisborg, USA) via a tether and electrical swivel (Stoelting Co, Illinois, USA), allowing free movement of the animal within the recording enclosure. The two cortical field-potential channels were digitized at 10000 samples/s (CED Power 1401, Cambridge, England), high- and lowpass filtered at 1 and 2500 Hz, respectively, and 50-Hz notch-filtered. The data were

displayed and recorded continuously on computer using Spike2 software (CED, Cambridge, England). The animals were video-recorded during all sessions to aid offline sleep-staging (described below). The video was synchronized with the electrophysiological recordings. Data were collected for up to six hours while the animals slept naturally.

9.2.4.4 Sleep staging

Sleep-staging was performed offline using accepted electrophysiological and behavioral criteria [44]. Slow-wave sleep (SWS) was characterized by a large-voltage, low-frequency ECoG waveform and regular respiratory pattern (observed on video). During SWS, the rats typically lay on their abdomen in a reclined posture.

Rapid eye movement (REM) sleep was characterized by a low-voltage, high-frequency ECoG waveform, and a respiratory pattern that was irregular, with frequent short apneas. REM sleep was confirmed by the observation of phasic phenomena such as eye movements and whisker twitches (observed on video) [44]. The rats often assumed a curled posture before entering REM sleep. Transitions from SWS to REM sleep were identified offline; two minutes of ECoG spanning each transition point were extracted for later analysis.

9.3 Results

The numerical model was implemented in MATLAB (Mathworks, Natick, MA, USA), simulating a 2×2 -cm square of cortex on a 16×16 grid with toroidal boundaries. We used a time-step of $50 \mu\text{s}$, chosen sufficiently small to ensure numerical stability. All grid points were driven by small-amplitude spatiotemporal white noise to simulate nonspecific (unstructured) flux activity from the subcortex. The primary output was the time-course of the mean-soma potential at selected grid points on the cortical sheet.

The soma-voltage predictions for the effect of neuromodulator-induced changes in excitability (ΔV_e^{rest}), and synaptic efficiency (λ), are illustrated in the manifold of equilibrium states in Fig. 9.1. Superimposed on the figure is a gray-arrowed hypothetical trajectory that tracks the influence of increasing cholinergic tone occurring during SWS-to-REM transition. The voltage-vs-time graphs show typical samples of model-generated “pseudoECoG” time-series at three selected ($\lambda, \Delta V_e^{\text{rest}}$) coordinates representing (a) slow-wave sleep (SWS); (b) intermediate sleep (IS); and (c) REM sleep.

With no cholinergic input, the SWS pattern (a) is associated with a slow cycling (~ 0.5 to 2 Hz) between the “up” (activated, upper stable region of the manifold) and “down” (quiescent, lower stable region) states (Fig. 9.1, area “SW”).

The effect of the increasing acetylcholine is modeled as a depolarizing drift of the resting membrane potential V_e^{rest} , a slight decrease in EPSP gain, and a loss of

frequency adaptation [13]. With increasing cholinergic tone, the trajectory moves to the right to a point where the up-states are close to the area in the phase space where an ~ 8 -Hz oscillatory state exists (shaded region in Fig. 9.1). At the upper-branch stability boundary, a subcritical Hopf bifurcation occurs [48]. Just beyond this point, the up-state is no longer stable (the real part of the dominant eigenvalue is positive), so cortical excursions to the upper-state lead to oscillations in the theta-frequency band. PseudoECoG time-series generated in this unstable region show spectral features characteristic of intermediate sleep: simultaneous delta and theta oscillations (Fig. 9.1, area “IS”; time-series (b)). The delta oscillation arises from the continuing presence of the up- and down-states, and the theta oscillation from the instability of the upper branch.

As the effects of the cholinergic modulation increase further, the pseudocortex eventually becomes so depolarized that only the up-state is available. The cortex now acts as an ~ 8 -Hz narrow-band filter of the nonspecific white noise input; this is our model’s representation of the REM theta-oscillation state (Fig. 9.1, area “REM”; time-series (c)).

Because we were unable to locate descriptions in the research literature for ECoG spectra at the SWS-to-REM transition, we elected to compare our model-generated spectra with those obtained from our ECoG recordings of sleep-transitioning rats. We computed time–frequency spectrograms for the model time-series (Fig. 9.2(a)) and for the rat ECoG recordings (Fig. 9.2(b)), and also calculated time–frequency coscalograms showing the spectral coherence between a pair of adjacent grid positions on the pseudocortex (Fig. 9.3(a)), comparing this with the spectral coherence between the pair of electrodes comprising the stereotrode that sensed rat ECoG activity (Fig. 9.3(b)).¹

The spectrograms (Fig. 9.2(a, b)) and coscalograms (Fig. 9.3(a, b)) both show predominant delta activity in SWS, appearance of co-existing theta activity in IS, and abrupt loss of delta activity marking the start of REM sleep.

The two-channel coherence scalograms of Fig. 9.3 exhibit distinct frequency banding. The peak frequency of the theta oscillation in the model (Fig. 9.3(a)) starts at ~ 4.5 Hz in intermediate sleep, increasing to ~ 6.5 Hz at the transition into REM, while the rat data show a broader low-frequency spectrum with transient tongues of coherent activity that extend almost into the theta range.

Table 9.2 compares the rat and model-generated ECoG data in terms of the mean and standard deviation for two-point wavelet coherence in the delta and in the theta wavebands. Coherences for both rat and simulated data exhibit similar trends across the transition from slow-wave sleep to REM sleep: both show a more than fourfold *decrease* in delta-band coherence, simultaneous with a fourfold *increase* in theta-band coherence. Across the three sleep stages, the absolute difference in coherences between rat and model data is better than 0.2 for delta-band, and better than 0.1 for theta-band. These coherence trends are illustrated in Fig. 9.4.

¹ See Appendix (Sects 9.5.2 and 9.5.3) for details of data processing, and calculation of coherence estimates from the Morlet wavelet transform.

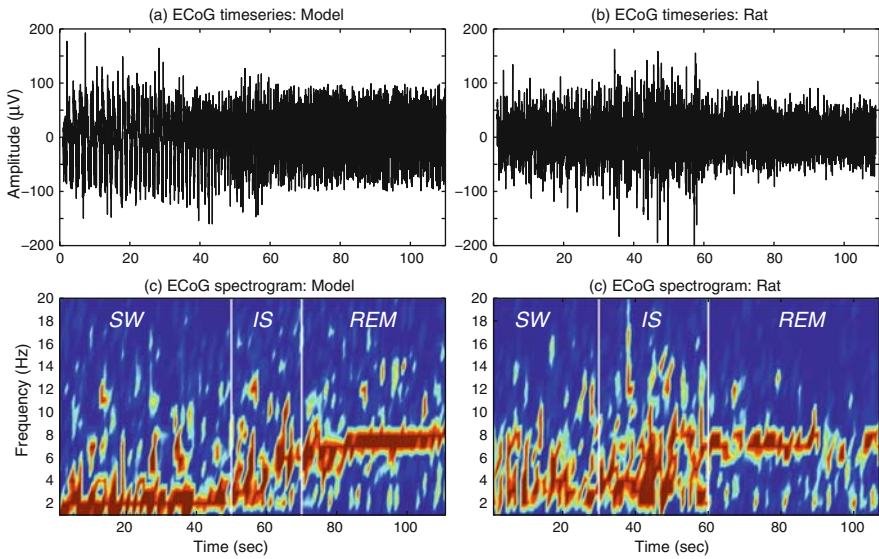


Fig. 9.2 [Color plate] Time-series and spectrograms of the model pseudoECoG signal (left), and of a typical example of rat ECoG (right) across the transition from slow-wave to REM sleep (*SW* = slow wave sleep; *IS* = intermediate sleep; *REM* = REM sleep). In both spectrograms, theta-band (5–8 Hz) activity first appears during early IS, while delta-band activity (1–4 Hz) is lost by the end of IS.

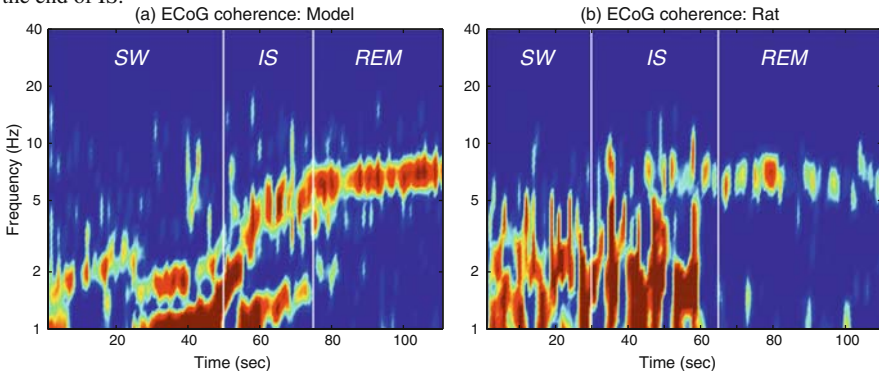


Fig. 9.3 [Color plate] Two-point temporal-coherence for two channels of pseudoECoG generated by the mean-field cortical model (left), compared with two-point coherence for rat stereotrope ECoG recording (right). Coherence is calculated using the Morlet continuous-wavelet transform (see Eq. (9.17)). In both model and experiment, there are coherent oscillations in theta- and delta-bands during the IS transition into REM sleep. (The nonlinear frequency axis is derived from the inverse of the wavelet-scale axis, and is thus distorted by the reciprocal transformation.)

9.4 Discussion

Most current neurobiological modeling of changes in cortical state involves simulation of various ion currents in assemblies of discrete Hodgkin–Huxley or

Table 9.2 Comparison of changes in two-point wavelet coherence (mean (SD)) for measured rat ECoG versus simulated pseudoECoG generated by the numerical model

Sleep stage	Delta band (1–4 Hz)		Theta band (5–8 Hz)	
	Rat	Model	Rat	Model
Slow-wave sleep	0.60 (0.02)	0.49 (0.06)	0.07 (0.06)	0.09 (0.04)
Intermediate sleep	0.48 (0.03)	0.63 (0.10)	0.28 (0.05)	0.22 (0.07)
REM sleep	0.14 (0.01)	0.09 (0.04)	0.29 (0.05)	0.36 (0.04)

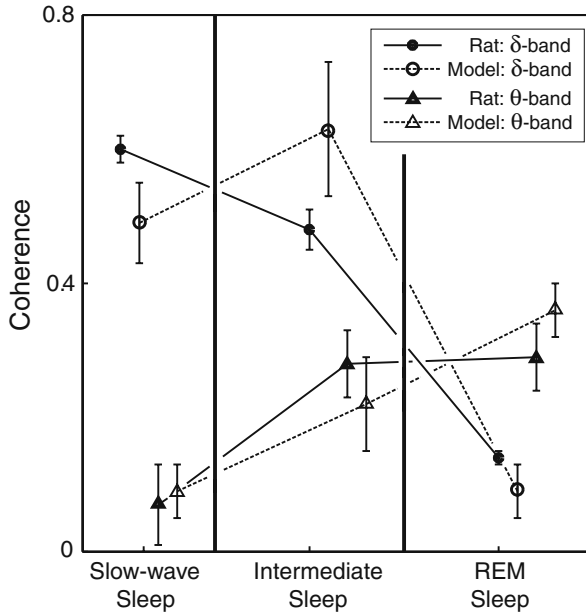


Fig. 9.4 Changes in two-point wavelet coherence across the SW-to-REM sleep transition, comparing recorded rat ECoG with model-generated ECoG. See Table 9.2 for coherence values.

integrate-and-fire neurons—the “neuron-by-neuron” approach [1, 6]. In contrast, the continuum philosophy assumes that, on average, neighboring neurons have very similar activity, so neural behavior can be approximated by population means that have been averaged over a small area of cortex. This assumption is in agreement with measured anatomic and functional spatial correlations [35]. The continuum method makes tractable the problem of quantifying global cortical phenomena, such as states of sleep, general anesthesia, and generalized seizures. Since the averaged electrical activity of populations of neurons is a commonly-measured experimental signal (ECoG), the accuracy of continuum models can be verified directly from clinical and laboratory observations, and many of the global phenomena of the cortex can be explained simply using the continuum approach. For example, if the cortex is envisaged as a network of single neurons, it is hard to explain the widespread

zero-lag spatial synchrony detected in SWS oscillations by Volgushev and colleagues [45]. In that paper, Volgushev postulated gap-junction coupling as the origin of the tight synchrony. In contrast, when the continuum formulation is used to model SWS, the high spatial synchrony arises naturally from the present set of cortical equations that do not contain diffusive couplings.

We have focused on a single question: “What is the basis for the abrupt changes in cortical activity that occur during the SWS-to-REM sleep transition?” There are two opposed explanations. One possibility is that there might be a massive, sudden increase in subcortical excitatory input into the cortex. In this scenario, the underlying cause of the change occurs *subcortically*, and the cortex is responding *linearly* to that input—this is the picture that is implicit in most earlier qualitative descriptions of the SWS-to-REM transition.

Our modeling supports the contrary view. We suggest that there is only a modest change in subcortical input occurring over a time-course of a few minutes, but that this modest change in stimulus triggers a secondary *nonlinear change in cortical self-interaction*, causing an abrupt jump to a new mode of electrophysiological (and cognitive) behavior. This cortical change of state is analogous to a phase-transition in physics, and can be described as a bifurcation in dynamical systems theory.

The earliest semi-quantitative model for SWS–REM cycling was developed by Hobson [15] who suggested that the changes in sleep state are driven by cycling in the brainstem, alternating between monoaminergic and cholinergic states. This theory did not address how the brainstem cycling determines the ECoG cortical response. More recently, Lu and others [24] have postulated that a bistable (“flip-flop”) system exists in the brainstem (the mesopontine tegmentum) to control SWS–REM transitions. The flip-flop is driven by mutual negative-feedback between “REM-on” and “REM-off” GABAergic areas. However, the primary effector pathways between the REM-on/REM-off flip-flop and the cortex were not well described. Part of the REM-on area contains glutamatergic neurons that form a *localized* ascending projection to the medial septum area of the basal forebrain, and hence to the hippocampus; thus the widespread *global* cortical activation seen in REM sleep is not explained. There is a weight of other evidence suggesting the pre-eminent role of cholinergic activation as the final common pathway of REM-sleep cortical arousal [5, 7].

The origin of the cortical theta-oscillation in the REM-state is the source of some debate. It had been assumed that the neocortical theta arises from volume conduction of the strong theta-oscillation that is observed in the hippocampus during REM sleep. However, there is evidence that the neocortical theta-rhythm may arise from the neocortex, *independent* of the hippocampus [3, 5, 20]. Cantero *et al.* [4] showed that cortical and hippocampal theta-rhythms often have different phases, and concluded that there are many different generators of theta-rhythm in the brain; the hippocampal theta is in turn dependent on the degree of activation of various brainstem structures [29].

Our theoretical model demonstrates that it is possible for an 8-Hz rhythm in the neocortex to emerge naturally from the internal dynamics of the equations. This oscillation derives from the lags introduced into the system by the inhibitory dendritic

input into the pyramidal neuronal population. Whether this is the source of all theta-oscillations observed during REM sleep in rats remains an open question. One problem with our model is that the amplitude of the theta-oscillation is sometimes as large as the slow oscillation, making the SWS-to-REM transition less clear on the pseudoECoG timeseries—although the transition remains obvious in the spectral views provided by the spectrogram and coscalogram.

As we have confirmed in the present study, one of the characteristics of the SWS–REM transition is high temporal coherence—in particular frequency bands—for spatially-separated electrodes. In rats, coherent oscillations have been observed across widespread areas of the brain that include not only cortex, but also thalamus, hippocampus and striatum [10]. Interestingly, the pattern of spindle activity observed during IS resembles that of forebrain preparations completely isolated from the brainstem [12]. In addition, examination of the amplitudes of sensory evoked-potentials shows that IS is associated with the lowest level of thalamocortical transfer of any sleep state. Thus IS is the most “introspective” of all sleep states, consistent with a role for IS in functional “in-house” coupling to support organization and integration of information between separated brain regions.

The continuum model provides a plausible theoretical basis for the phenomenon of intermediate sleep in rats. However, the model requires further experimental validation to test its predictions. We envisage a detailed and systematic experimental exploration of the model parameter space, using *in vitro* cortical-slice methods to manipulate the position of the cortical dynamics on the equilibrium manifold. Here is an example of the approach: It is known that the addition of triazolam (a GABAergic drug) markedly increases the duration of the IS stage, at the expense REM sleep [11]. We tested this finding against our continuum model by running simulations with enhanced GABAergic effect. We found that the duration of IS increases linearly with IPSP (inhibitory postsynaptic potential) *decay-time*, and increases markedly with even modest increases in the IPSP *magnitude*. Conversely, a drug which shortens IPSP decay-time will reduce the extent of the unstable “tongue” on the edge of the upper branch of the manifold, and, with sufficient reduction, should eliminate the IS stage entirely. This is an unambiguous and testable prediction.

9.5 Appendix

9.5.1 Mean-field cortical equations

The model describes interactions between cortical populations of excitatory pyramidal neurons (subscript e) and inhibitory interneurons (subscript i).² We use a left-to-right double-subscripting convention so that subscript ab (where a and b are labels standing for either e or i) implies $a \rightarrow b$, that is, the direction of transmission

² Note that we have not included a representation of the thalamus in the model, because the slow oscillation of sleep can be generated in the cortex alone—without thalamic input [33, 41, 45].

in the synaptic connections is from the presynaptic nerve a to postsynaptic nerve b . Superscript “sc” indicates subcortical input that is independent of the cortical membrane potential.

The time-evolution of the population-mean membrane potential (V_a) in each neuronal population, in response to synaptic input $\rho_a \Psi_{ab} \Phi_a$, is given by,

$$\tau_e \frac{\partial V_e}{\partial t} = V_e^{\text{rest}} + \Delta V_e^{\text{rest}} - V_e + \lambda \rho_e \Psi_{ee} \Phi_{ee} + \rho_i \Psi_{ie} \Phi_{ie}, \quad (9.5)$$

$$\tau_i \frac{\partial V_i}{\partial t} = V_i^{\text{rest}} - V_i + \lambda \rho_e \Psi_{ei} \Phi_{ei} + \rho_i \Psi_{ii} \Phi_{ii}, \quad (9.6)$$

where τ_a are the time constants of the neurons, and ρ_a are the strengths of the postsynaptic potentials (proportional to the total charge transferred per PSP event). Here we modulate the resting-voltage offset ΔV_e^{rest} and the synaptic-gain scalefactor λ as set out in Eqs (9.1–9.3). The Ψ_{ab} are weighting functions that allow for the effects of AMPA and GABA reversal potentials V_a^{rev} ,

$$\Psi_{ab} = \frac{V_a^{\text{rev}} - V_b}{V_a^{\text{rev}} - V_a^{\text{rest}}}. \quad (9.7)$$

The Φ_{ab} are synaptic-input spike-rate fluxes described by Eqs (9.8–9.9),

$$\left(\frac{\partial^2}{\partial t^2} + 2\gamma_{eb} \frac{\partial}{\partial t} + \gamma_{eb}^2 \right) \Phi_{eb} = \gamma_{eb}^2 \left(N_{eb}^\alpha \phi_{eb} + N_{eb}^\beta Q_e + \phi_{eb}^{\text{sc}} \right), \quad (9.8)$$

$$\left(\frac{\partial^2}{\partial t^2} + 2\gamma_{ib} \frac{\partial}{\partial t} + \gamma_{ib}^2 \right) \Phi_{ib} = \gamma_{ib}^2 \left(N_{ib}^\beta Q_i + \phi_{ib}^{\text{sc}} \right), \quad (9.9)$$

where γ_{ab} are the synaptic rate-constants, N^α are the number of long-range connections, and N^β the number of local, within-macrocolumn connections. The spatial interactions between macrocolumns are described by damped wave equations,

$$\left(\frac{\partial^2}{\partial t^2} + 2v\Lambda_{eb} \frac{\partial}{\partial t} + v^2\Lambda_{eb}^2 - v^2\nabla^2 \right) \phi_{eb} = v^2\Lambda_{eb}^2 Q_e, \quad (9.10)$$

where v is the mean axonal velocity, and $1/\Lambda_{eb}$ is the characteristic length-scale for axonal connections.

The population firing-rate of the neurons is related to the population-mean soma potential by a sigmoidal mapping,

$$Q_a(V_a) = \frac{Q_a^{\text{max}}}{1 + \exp[-\pi(V_a - \theta_a)/\sqrt{3}\sigma_a]} \quad (9.11)$$

where θ_a is the population-average threshold voltage, and σ_a is its standard deviation. The parameters and ranges used in our simulations are listed in Table 9.1.

9.5.2 Comparison of model mean-soma potential and experimentally-measured local-field potential

In order to translate from a grid simulation of soma potential to a pseudoECoG, we introduce three virtual electrodes that sample the fields from different sets of neurons. The first virtual electrode serves as a “common reference” that samples the local field $V_{j,k}$ from all grid-points (j,k) equally, giving a reference voltage $V^{\text{ref}}(t) = \frac{1}{N^2} \sum_{j=1}^N \sum_{k=1}^N V_{j,k}(t)$, where $N = 16$ in our simulations. This construction is intended to be broadly equivalent to the common reference electrodes utilized in our rat experiments—these were located bilaterally over the parietal cortex, responding to the local field potential across a wide spatial extent of neurons.

The other two virtual electrodes, numbered (1) and (2), we assume to be much more localized, sampling the field from a pair of adjacent grid-points (j,k) , $(j+1,k)$ in the simulation, but each containing a small voltage contribution, say 1%, coming from the spatial average over all 256 grid-points, leading to a pair of electrode potentials, relative to ground, of

$$\begin{aligned} V^{(1)}(t) &= V_{j,k}(t) + 0.01 V^{\text{ref}}(t), \\ V^{(2)}(t) &= V_{j+1,k}(t) + 0.01 V^{\text{ref}}(t). \end{aligned}$$

The two pseudoECoG voltages are then formed as the respective differences between $V^{(1),(2)}$ and V^{ref} ,

$$\text{pECoG}^{(1)}(t) = V_{j,k}(t) - 0.99 V^{\text{ref}}(t), \quad (9.12)$$

$$\text{pECoG}^{(2)}(t) = V_{j+1,k}(t) - 0.99 V^{\text{ref}}(t). \quad (9.13)$$

We have found that this subtractive fraction of 99% of the spatial-average soma potential produces physically reasonable pseudoECoG traces which have a strong contribution from the local voltage fluctuations at the specified grid point, but retain a weak contribution from the global activity that is common to the entire grid.

To reduce memory requirements, grid-simulation soma potentials were recorded every 250 timesteps with $\Delta t = 50 \mu\text{s}$, giving an effective sampling rate of $1/(250\Delta t) = 80 \text{ s}^{-1}$. A Butterworth highpass filter was applied to remove fluctuation energy below 0.5 Hz. ECoG voltages recorded from rat cortex were bandpass filtered by the acquisition hardware to eliminate spectral content outside the range 1–2500 Hz. The effective sampling rate was reduced from $10\,000 \text{ s}^{-1}$ to 80 s^{-1} using `decimate` to lowpass filter the time-series to 32 Hz, then subsample by a factor of 125.

9.5.3 Spectrogram and coscalogram analysis

To track the spectral changes in ECoG voltage activity over the course of the SWS-to-REM transition, we computed Hanning-windowed spectrograms with a 1-Hz

resolution using the MATLAB `pwelch` function. This spectral analysis was applied to the rat ECoG time-series (Fig. 9.2(b)), and also to the pseudoECoG time-series generated by our mean-field numerical simulations (Fig. 9.2(a)).

The synchronous interactions *between* the two ECoG channels were quantified using wavelet coherence [19, 21]. Because optimal time–frequency localization was required, we devised a new coherence measure—based on the Morlet continuous wavelet transform—to investigate the spatiotemporal relationships of the two ECoG series during the rat transition into sleep.

Given a time-function $x(t)$, its continuous wavelet transform (CWT) is defined,

$$W(s, \tau) = \frac{1}{\sqrt{s}} \int x(t) \Psi^* \left(\frac{t - \tau}{s} \right) dt, \quad (9.14)$$

where s and τ denote the temporal scale and translation respectively; $W(s, \tau)$ are the wavelet coefficients; $\Psi(t)$ is the wavelet function; and superscript (*) denotes complex conjugation. In this study, a Morlet wavelet function,

$$\Psi_0(u) = \pi^{-1/4} e^{i\omega_0 u} e^{-\frac{1}{2}u^2}, \quad (9.15)$$

is applied. Here, ω_0 is a nondimensional central angular frequency; a value of $\omega_0 = 8$ is considered optimal for good time–frequency resolution [9]. Because the Morlet wavelet retains amplitude and phase information, the degree of synchronization between neural activity simultaneously recorded at two sites can be measured.

Given a pair of ECoG time-series, X and Y , their Morlet wavelet transforms are denoted by $W_X(s, n)$ and $W_Y(s, n)$, respectively, where s is the scale and n the time-index. Their coscogram is defined

$$|W_{XY}(s, n)| \equiv |W_X(s, n) W_Y^*(s, n)|. \quad (9.16)$$

The coscogram illustrates graphically the coincident events between two time-series, at each scale s and at the each time index n . To quantify the degree of synchronization between the two time-series, we compute the wavelet coherence,

$$[\text{coh}(s, n)]^2 = \frac{|\langle s^{-1} W_{XY}(s, n) \rangle|^2}{\langle s^{-1} |W_{XX}(s, n)|^2 \rangle \langle s^{-1} |W_{YY}(s, n)|^2 \rangle}. \quad (9.17)$$

The coherence ranges from 0 to 1, and provides an accurate representation for the covariance between two EEG time-series. The angle-brackets $\langle \cdot \rangle$ indicate smoothing in time and scale; the internal factor s^{-1} is required to convert to an energy density. The smoothing in time is achieved using a Gaussian function $\exp(-\frac{1}{2}(t/s)^2)$; the smoothing in scale is done using a boxcar filter of width 0.6 (see Ref. [42]). Because of the smoothing, wavelet coherence effectively provides an ensemble averaging localized in time, thereby reducing the variance from noise [19].

References

1. Bazhenov, M., Timofeev, I., Steriade, M., Sejnowski, T.J.: Model of thalamocortical slow-wave sleep oscillations and transitions to activated states. *J. Neurosci.* **22**(19), 8691–704 (2002)
2. Benington, J.H., Kodali, S.K., Heller, H.C.: Scoring transitions to REM sleep in rats based on the EEG phenomena of pre-REM sleep: an improved analysis of sleep structure. *Sleep* **17**(1), 28–36 (1994)
3. Borst, J., Leung, L.W., MacFabe, D.: Electrical activity of the cingulate cortex. ii. cholinergic modulation. *Brain Res* **407**, 81–93. (1987), doi:10.1016/0006-8993(87)91221-2
4. Cantero, J., Atienza, M., Stickgold, R., Kahana, M., Madsen, J., Kocsis, B.: Sleep-dependent theta oscillations in the human hippocampus and neocortex. *J. Neurosci.* **23**(34), 10897–10903 (2003)
5. Cape, E., Jones, B.: Effects of glutamate agonist versus procaine microinjections into the basal forebrain cholinergic cell area upon gamma and theta EEG activity and sleep-wake state. *Eur. J. Neurosci.* **12**, 2166–2184 (2000), doi:10.1046/j.1460-9568.2000.00099.x
6. Compte, A., Sanchez-Vives, M.V., McCormick, D.A., Wang, X.J.: Cellular and network mechanisms of slow oscillatory activity (<1 Hz) and wave propagations in a cortical network model. *J. Neurophys.* **89**(5), 2707–2725 (2003), doi:10.1152/jn.00845.2002
7. Datta, S., Siwek, D.F.: Excitation of the brainstem pedunculopontine tegmentum cholinergic cells induces wakefulness and REM sleep. *J. Neurophys.* **77**(6), 2975–2988 (1997)
8. El Mansari, M., Sakai, K., Jouvet, M.: Unitary characteristics of presumptive cholinergic tegmental neurons during the sleep-waking cycle in freely moving cats. *Exp. Brain Res.* **76**, 519–529 (1989), doi:10.1007/BF00248908
9. Farge, M.: Wavelet transforms and their applications to turbulence. *Ann. Rev. Fluid. Mech.* **24**, 395–457 (1992), doi:10.1146/annurev.fl.24.010192.002143
10. Gervasoni, D., Lin, S.C., Ribeiro, S., Soares, E.S., Pantoja, J., Nicolelis, M.A.: Global forebrain dynamics predict rat behavioral states and their transitions. *J. Neurosci.* **24**(49), 11137–11147 (2004), doi:10.1523/jneurosci.3524-04.2004
11. Gottesmann, C.: The transition from slow-wave sleep to paradoxical sleep: Evolving facts and concepts of the neurophysiological processes underlying the intermediate stage of sleep. *Neurosci. Biobehav. Rev.* **20**(3), 367–387 (1996), doi:10.1016/0149-7634(95)00055-0
12. Gottesmann, C., Gandolfo, G., Arnaud, C., Gauthier, P.: The intermediate stage and paradoxical sleep in the rat: Influence of three generations of hypnotics. *Eur. J. Neurosci.* **10**(2), 409–14 (1998), doi:10.1046/j.1460-9568.1998.00069.x
13. Hasselmo, M., McGaughy, J.: High acetylcholine levels set circuit dynamics for attention and encoding and low acetylcholine levels set dynamics for consolidation. *Prog. Brain Res.* **145**, 207–231 (2004), doi:10.1016/S0079-6123(03)45015-2
14. Hill, S., Tononi, G.: Modeling sleep and wakefulness in the thalamocortical system. *J. Neurophysiol.* **93**, 1671–1698 (2005), doi:10.1152/jn.00915.2004
15. Hobson, J.A., McCarley, R.W., Wyzinski, P.W.: Sleep cycle oscillation: Reciprocal discharge by two brainstem neuronal groups. *Science* **189**(4196), 55–58 (1975), doi:10.1126/science.1094539
16. Hobson, J.A., Pace-Schott, E.F.: The cognitive neuroscience of sleep: Neuronal systems, consciousness and learning. *Nat. Rev. Neurosci.* **3**(9), 679–693 (2002), doi:10.1038/nrn915
17. Holcman, C., Tsodyks, M.: The emergence of up and down states in cortical networks. *PLoS. Comput. Biol.* **2**(3), 174–181 (2006), doi:10.1371/journal.pcbi.0020023
18. Jones, B.: Activity, modulation and role of basal forebrain cholinergic neurons innervating the cerebral cortex. *Prog. Brain Res.* **145**, 157–169 (2004), doi:10.1016/S0079-6123(03)45011-5
19. Lachaux, J.P., Rudrauf Lutz, A., Cosmelli, D., Le Van Quyen, M., Martinerie, J., Varela, F.: Estimating the time-course of coherence between single-trial brain signals: an introduction to wavelet coherence. *Clin. Neurophysiol.* **32**(3), 157–174 (2002), doi:10.1016/S0987-7053(02)00301-5

20. Lee, M., Hassani, O., Alonso, A., Jones, B.: Cholinergic basal forebrain neurons burst with theta during waking and paradoxical sleep. *J. Neurosci.* **25**(17), 4365–4369. (2005), doi:10.1523/jneurosci.0178-05.2005
21. Leinekugel, X., Khazipov, R., Cannon, R., Hirase, H., Ben-Ari, Y., Buzsáki, G.: Correlated bursts of activity in the neonatal hippocampus in vivo. *Science* **296**, 2049–2052 (2002), doi:10.1126/science.1071111
22. Liley, D., Cadusch, P., Wright, J.: A continuum theory of electro-cortical activity. *Neurocomp.* **26-27**, 795–800 (1999), doi:10.1016/S0925-2312(98)00149-0
23. Linster, C., Hasselmo, M.E.: Neuromodulation and the functional dynamics of piriform cortex. *Chem. Senses* **26**(5), 585–594 (2001), doi:10.1093/chemse/26.5.585
24. Lu, J., Sherman, D., Devor, M., Saper, C.: A putative flip-flop switch for control of REM sleep. *Nature* **441**, 583–591. (2006), doi:10.1038/nature04767
25. Mandile, P., Vescia, S., Montagnese, P., Romano, F., Giuditta, A.: Characterization of transition sleep episodes in baseline EEG recordings of adult rats. *Physiol. Behav.* **60**(6), 1435–9 (1996), doi:10.1016/S0031-9384(96)00301-0
26. Massimini, M., Huber, R., Ferrarelli, F., Hill, S., Tononi, G.: The sleep slow oscillation as a traveling wave. *J. Neurosci.* **24**(31), 6862–6870 (2004), doi:10.1523/jneurosci.1318-04.2004
27. Metherate, R., Cox, C.L., Ashe, J.H.: Cellular bases of neocortical activation: modulation of neural oscillations by the nucleus basalis and endogenous acetylcholine. *J. Neurosci.* **12**(12), 4701–4711 (1992)
28. Morrissey, M.J., Anch, A.M., Duntley, S.P.: An evaluation of the use of seizure prone rats when investigating intermediate stage sleep. *J. Neurosci. Meth.* **143**(2), 159–162 (2005), doi:10.1016/j.jneumeth.2004.09.026
29. Nunez, A., Cervera-Ferri, A., Olucha-Bordonau, F., Ruiz-Torna, A., Teruel, V.: Nucleus incertus contribution to hippocampal theta rhythm generation. *Eur. J. Neurosci.* **23**, 2731–2738 (2006), doi:10.1111/j.1460-9568.2006.04797.x
30. Pace-Schott, E.F., Hobson, J.A.: The neurobiology of sleep: genetics, cellular physiology and subcortical networks. *Nat. Rev. Neurosci.* **3**(8), 591–605 (2002)
31. Porkka-Heiskanen, T., Alanko, L., Kalinchuk, A., Stenberg, D.: Adenosine and sleep. *Sleep Med. Rev.* **6**(4), 321–332 (2002), doi:10.1053/smr.2001.0201
32. Saito, H., Sakai, K., Jouvet, M.: Discharge patterns of the nucleus parabrachialis lateralis neurons of the cat during sleep and waking. *Brain Res.* **134**(1), 59–72 (1977), doi:10.1016/0006-8993(77)90925-8
33. Sanchez-Vives, M.V., McCormick, D.A.: Cellular and network mechanisms of rhythmic recurrent activity in neocortex. *Nat. Neurosci.* **3**(10), 1027–1034 (2000), doi:10.1038/79848
34. Saper, C., Scammell, T., Lu, J.: Hypothalamic regulation of sleep and circadian rhythms. *Nature* **437**, 1257–1263 (2005), doi:10.1038/nature04284
35. Shepherd, G., Stepanyants, A., Bureau, I., Chklovskii, D., Svoboda, K.: Geometric and functional organization of cortical circuits. *Nat. Neurosci.* **8**(6), 782–791 (2005), doi:10.1038/nn1447
36. Shu, Y., Hasenstaub, A., McCormick, D.A.: Turning on and off recurrent balanced cortical activity. *Nature* **423**(6937), 288–293 (2003), doi:10.1038/nature01616
37. Steriade, M., Datta, S., Pare, D., Oakson, G., Curro Dossi, R.C.: Neuronal activities in brainstem cholinergic nuclei related to tonic activation processes in thalamocortical systems. *J. Neurosci.* **10**(8), 2541–2559 (1990)
38. Steriade, M., Timofeev, I., Grenier, F.: Natural waking and sleep states: A view from inside neocortical neurons. *J. Neurophys.* **85**(5), 1969–1985 (2001)
39. Steyn-Ross, D.A., Steyn-Ross, M.L., Sleigh, J.W., Wilson, M.T., Gillies, I.P., Wright, J.J.: The sleep cycle modelled as a cortical phase transition. *J. Biol. Phys.* **31**, 547–569 (2005), doi:10.1007/s10867-005-1285-2
40. Steyn-Ross, M.L., Steyn-Ross, D.A., Sleigh, J.W., Wilson, M.T., Wilcocks, L.C.: Proposed mechanism for learning and memory erasure in a white-noise-driven sleeping cortex. *Phys. Rev. E* **72**, 061910 (2005), doi:10.1103/PhysRevE.72.061910

41. Timofeev, I., Grenier, F., Steriade, M.: Impact of intrinsic properties and synaptic factors on the activity of neocortical networks in vivo. *J. Physiology-Paris* **94**(5-6), 343–355 (2000), doi:10.1016/S0928-4257(00)01097-4
42. Torrence, C., Webster, P.J.: Interdecadal changes in the ENSO-monsoon system. *J. Climate* **12**(8), 2679–2690 (1999), doi:10.1175/1520-0442(1999)012<2679:icitem>2.0.CO;2
43. Tsodyks, M.V., Markram, H.: The neural code between neocortical pyramidal neurons depends on neurotransmitter release probability. *P. Natl. Acad. Sci. USA* **94**(2), 719–723 (1997), doi:10.1073/pnas.94.2.719
44. van Beteray, J.N., Vossen, J.M., Coenen, A.M.: Behavioural characteristics of sleep in rats under different light/dark conditions. *Physiol. Behav.* **50**(1), 79–82 (1991), doi:10.1016/0031-9384(91)90501-E
45. Volgushev, M., Chauvette, S., Mukovski, M., Timofeev, I.: Precise long-range synchronization of activity and silence in neocortical neurons during slow-wave sleep. *J. Neurosci.* **26**(21), 5665–5672 (2006), doi:10.1523/jneurosci.0279-06.2006
46. Wilson, H.R., Cowan, J.D.: Excitatory and inhibitory interactions in localized populations of model neurons. *Biophys. J.* **12**(1), 1–24 (1972)
47. Wilson, M.T., Sleigh, J.W., Steyn-Ross, D.A., Steyn-Ross, M.L.: General anaesthetic-induced seizures can be explained by a mean-field model of cortical dynamics. *Anesthesiology* **104**(3), 588–593 (2006), doi:10.1097/00000542-200603000-00026
48. Wilson, M.T., Steyn-Ross, M.L., Steyn-Ross, D.A., Sleigh, J.W.: Predictions and simulations of cortical dynamics during natural sleep using a continuum approach. *Phys. Rev. E* **72**(5), 051910 (2005), doi:10.1103/PhysRevE.72.051910
49. Wilson, M., Steyn-Ross, D., Sleigh, J., Steyn-Ross, M., Wilcocks, L., Gillies, I.: The K-complex and slow oscillation in terms of a mean-field cortical model. *J. Comput. Neurosci.* **21**, 243–257 (2006), doi:10.1007/s10827-006-7948-6
50. Wright, J.J., Liley, D.T.: Dynamics of the brain at global and microscopic scales: Neural networks and the EEG. *Behav. Brain Sci.* **19**, 285–320 (1996)